Journal of Power Sources 195 (2010) 257–262

Contents lists available at ScienceDirect

Journal of Power Sources

journal homepage: www.elsevier.com/locate/jpowsour

Thermal imaging of solid oxide fuel cell anode processes

Michael B. Pomfret[a], Daniel A. Steinhurst[b], David A. Kidwell[a], Jeffrey C. Owrutsky[a,*]

[a] Chemistry Division, U.S. Naval Research Laboratory, Washington, DC 20375, USA
[b] Nova Research Inc., Alexandria, VA 22308, USA

ARTICLE INFO

Article history:
Received 7 May 2009
Received in revised form 19 June 2009
Accepted 22 June 2009
Available online 30 June 2009

Keywords:
Thermal imaging
Solid oxide fuel cell
In situ optics
Hydrocarbon fuels

ABSTRACT

A Si-charge-coupled device (CCD), camera-based, near-infrared imaging system is demonstrated on Ni/yttria-stabilized zirconia (YSZ) fragments and the anodes of working solid oxide fuel cells (SOFCs). NiO reduction to Ni by H_2 and carbon deposition lead to the fragment cooling by $5 \pm 2\,^{\circ}C$ and $16 \pm 1\,^{\circ}C$, respectively. When air is flowed over the fragments, the temperature rises $24 \pm 1\,^{\circ}C$ as carbon and Ni are oxidized. In an operational SOFC, the decrease in temperature with carbon deposition is only $4.0 \pm 0.1\,^{\circ}C$ as the process is moderated by the presence of oxides and water. Electrochemical oxidation of carbon deposits results in a ΔT of $+2.2 \pm 0.2\,^{\circ}C$, demonstrating that electrochemical oxidation is less vigorous than atmospheric oxidation. While the high temperatures of SOFCs are challenging in many respects, they facilitate thermal imaging because their emission overlaps the spectral response of inexpensive Si-CCD cameras. Using Si-CCD cameras has advantages in terms of cost, resolution, and convenience compared to mid-infrared thermal cameras. High spatial (~0.1 mm) and temperature (~0.1 °C) resolutions are achieved in this system. This approach provides a convenient and effective analytical technique for investigating the effects of anode chemistry in operating SOFCs.

Published by Elsevier B.V.

1. Introduction

Solid oxide fuel cells (SOFCs) are promising devices for stationary or portable power and heat generation [1–5]. A primary advantage of SOFCs over other non-combustion energy sources is the ability of SOFCs to operate using complex fuels such as hydrocarbons or alcohols. SOFCs require high temperatures (>700 °C) to drive thermally activated oxide diffusion through the solid electrolyte [6,7], a condition that facilitates using high molecular weight fuels by effectively reforming fuels *in situ* [8–10], but presents material challenges in terms of device development for viable and durable commercial and military applications [5,11]. SOFCs designs must employ materials that maintain their chemical and structural integrity under extreme conditions for extended periods of time. Accomplishing these goals will require understanding the mechanisms of fuel utilization under various operating conditions as well as improved tracking of the structural and chemical transformations responsible for diminished membrane-electrode assembly (MEA) performance and device failure.

Understanding the complex chemistry of fuels at SOFC anodes under typical operating conditions has proven difficult [12–14]. Electrochemical methods such as voltammetry and electrochemical impedance spectroscopy are effective for quantifying cell performance [15,16], but not for identifying the local, chemical processes. *In situ* Raman and infrared (IR) spectroscopies and thermal imaging have begun to address these issues [13,17–23]. Thermal imaging has been demonstrated as a powerful technique for monitoring the spatial and thermal characteristics of SOFC cathode operation, providing far richer information than the traditional point measurement of a thermocouple [18,20].

In this study, near-IR (NIR) imaging with high spatial resolution is used to address the effects of flow composition on SOFC anode material – Ni/yttria-stabilized zirconia (YSZ) – by monitoring temperature changes of the anode surface. NIR thermography has proven to be a key tool in other systems [24–28]. Thermal gradients across the anode or other components of the SOFC could affect its performance or indicate spatially varying chemistry or material changes. Patterns of temperature variations or fluctuations may also precede anode failure, so this technique could potentially serve as a diagnostic for anode degradation. The emission from SOFCs extends to NIR wavelengths, which can be detected by Si-charge-coupled device (CCD) cameras because of the elevated operating temperatures. Being able to use Si-CCD cameras has distinct advantages in terms of cost, resolution, and convenience compared to mid-IR thermal (InSb, mercury cadium telluride, PtSi, etc.) cameras.

Two fuels – hydrogen and propane – are used to study thermal variations in time and position not only on Ni/YSZ fragments, but also on anodes of operating SOFCs. Propane is investigated to explore how carbon deposition and electrochemical oxidation affect the anode temperature. Fuels tend to reduce the tempera-

* Corresponding author. Tel.: +1 202 404 6352; fax: +1 202 404 8119.
E-mail address: jeff.owrutsky@nrl.navy.mil (J.C. Owrutsky).

0378-7753/$ – see front matter. Published by Elsevier B.V.
doi:10.1016/j.jpowsour.2009.06.072

ture while various oxidation processes tend to increase it. Carbon deposition cools Ni/YSZ surfaces, which occurs to a greater extent on Ni/YSZ fragments than on anodes of operational SOFCs. SOFCs supply oxides to the anode, which diminishes the temperature drop from carbon deposition. In the fragment study, changing the flow to air leads to heating as the Ni and carbon are oxidized. Electrochemical oxidation of carbon and Ni in functional SOFCs results in less heating than air flow on fragments. These results show the effects of using a hydrocarbon fuel and of electrochemical processes on SOFC anodes.

2. Materials and methods

2.1. Fuel cell construction

The custom-made, button cell SOFCs used in this study were obtained from Materials & Systems Research, Inc. (Salt Lake City, UT). The 25 mm diameter MEAs were supported by a ~1 mm thick, large grain, Ni/YSZ composite anode. Other layers included a small grain, Ni/YSZ 25 μm thick anode interlayer; a 20 μm thick YSZ electrolyte; a 25 μm thick, strontium-doped lanthanum manganate (LSM)/YSZ cathode interlayer; and a 50 μm thick LSM cathode. MEAs with the same dimensions have been previously structurally and electrochemically characterized [29].

Gold wires and platinum mesh were attached to the anodes and cathodes using Pt ink (Engelhard #6082). The wired disks were attached anode-side-out to a custom-built, 25.4 mm OD alumina tube (Sentrotech) assembly with zirconia paste (Aremco Products, Inc.). A 50.8 mm OD alumina tube surrounded the alumina-supported MEA and a 50.8 mm diameter, 3.175 mm thick sapphire window (Swiss Jewel Co.) was attached to one end of the outer alumina tube to contain the reactant and product gases while providing optical access to the anode. The rear of the assembly was sealed with RTV silicone-based paste (Permatex, Ultra-Copper). The assembled SOFC manifold was placed inside a tube furnace (Thermo Scientific, Model # F21135) and heated to the operating temperature of approximately 740 °C. A K-type thermocouple (Omega) was positioned on the outer surface of the outer alumina tube to provide a temperature reference. A schematic of the assembled fuel cell is shown in Fig. 1 and is similar in design to that of Ref. [20].

2.2. Gas flows

The anode-side flows were regulated with mass flow controllers (Tylan FC-260 and FC-280). The air supply for the cathode side was regulated with a needle valve and monitored with a mass flow meter (Tylan FM-360). Constant flows of ~150 sccm Ar and ~90 sccm air were delivered to the anode and cathode, respectively. A flow of 100 sccm H_2 was added to the anode for standard operation. To study the effects of C_3H_8 as a fuel, 100 sccm 1:9 C_3H_8:Ar mixture was added to the ~150 sccm Ar anode flow.

2.3. Electrochemical characterization

Cell polarization and linear sweep voltammetry measurements were monitored and conducted with a potentiostat (Pine Instrument Company, Model # AFCBP1). Cells were kept at open circuit voltage (OCV), which was typically ~−1.00 V for the majority of the experiments. A current of 200 mA was drawn from the cells to oxidize carbon deposits that resulted from C_3H_8 flow. Voltammetry measurements were made before and after each exposure to C_3H_8 fuel. Linear voltammetry sweeps with only H_2 as the fuel were conducted from OCV to 0.00 V cell potential at an effective scan rate of 50 mV s^{-1} and a step size of 5 mV. A typical voltammetry scan and calculated power density plot is shown in Fig. 2.

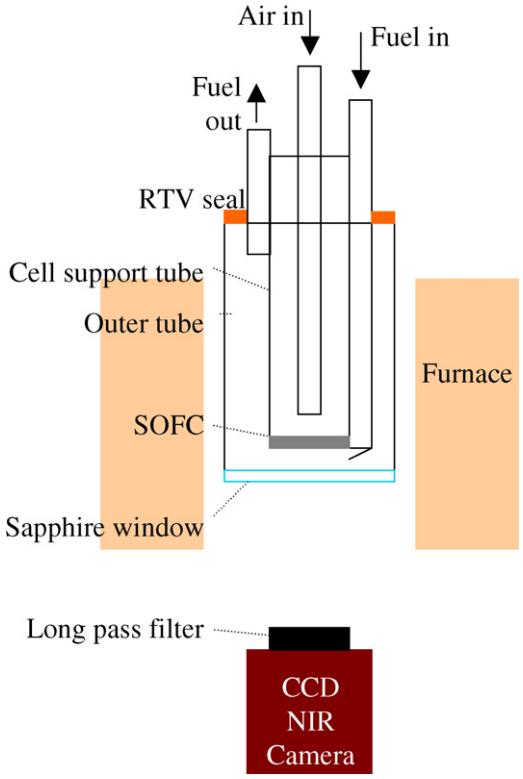

Fig. 1. SOFC imaging apparatus. Optical SOFC assembly used in this study.

2.4. Thermal imaging measurements

Thermal images were acquired with a 14-bit, 656 by 492 pixel, CCD camera (Allied Vision Technologies, Stingray F033B ASG) with a 75 mm-focal length telephoto lens (Edmund Optics, Techspec #A54-691) using collection software written in-house using LabView v8.5. A long-pass filter (Hoya R72), with a nominal cutoff wavelength of 720 nm was used to block emitted and ambient reflected visible light. The long-pass filter transmission convolved with the spectral response of the Si-CCD forms an effective broad bandpass filter between 720 and 1000 nm, with more sensitivity at shorter wavelengths. The images collected had a theoretical spatial resolution of ~0.1 mm in our set-up considering the lens, number of pixels, and one-meter separation between the cam-

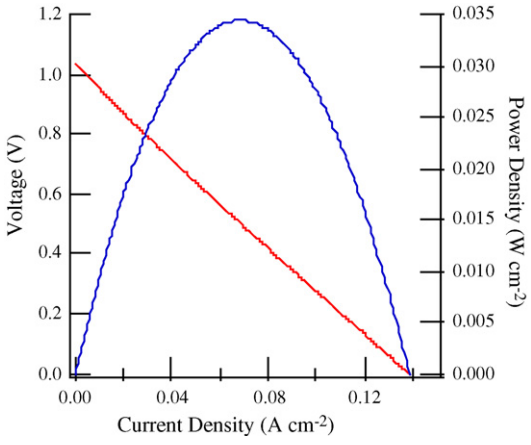

Fig. 2. Cell electrochemistry. A typical linear-sweep voltammetry scan (red) and the resulting power density curve (blue) of the SOFCs used in this study with H_2 as the fuel. (For interpretation of the references to color in this figure legend, the reader is referred to the web version of the article.)

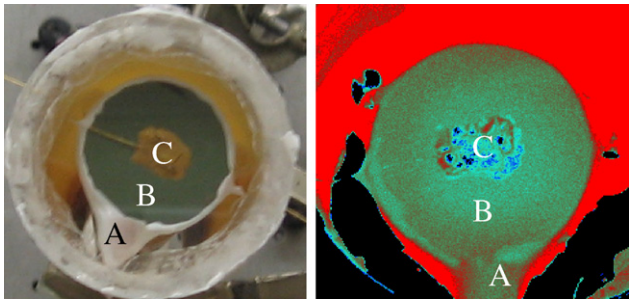

Fig. 3. Standard images of SOFC. Visual and NIR images of SOFCs showing (A) the fuel inlet, (B) the exposed Ni/YSZ anode, and (C) the Au current collector in both images.

era and the cell. A temperature resolution of ~0.1 °C was achieved based on the intensity, as controlled by the size of the aperture, and pixel depth. The intensity reading on the camera was calibrated to a thermocouple placed adjacent to the outer alumina tube. Intensity readings are taken at two temperatures (furnace temperatures of 750 and 800 °C) and a linear calibration was generated. All data were collected at 5 Hz, stored as intensity per pixel, and displayed as temperature-calibrated images and spatial profiles for real-time monitor/diagnosis. Data were post-processed into images (intensity or temperature-calibrated), digital movies, time series for selected regions of interest, and spatial profiles, as needed. An example of one of our cells and a labeled thermal image is shown in Fig. 3.

3. Results and discussion

Two studies are discussed below. First, the effects of H_2 and C_3H_8, and air flows on an unwired Ni/YSZ fragment are examined. Second, H_2 and C_3H_8 fuels are used in SOFCs to investigate how carbon deposition affects the temperature of operational SOFCs. Instead of using an air flow, the cells are polarized to oxidize the carbon and Ni in the cells with the electrochemical oxide flux.

3.1. Atmospheric oxidation, reduction, and carbon reactions

Preliminary experiments are conducted on SOFC fragments, without electrochemical control, to measure the effects of flow composition through the anode chamber. Initial measurements show no change in surface temperature when the Ar flow is varied from 100 to 200 sccm. Since all of our reactive flows are within this range, we do not attribute the observed temperature changes to convective cooling from fluctuations in flow. To study various reactions on the surface, a base flow of 100–150 sccm Ar is maintained throughout all experiments with the reactive gases added to the Ar flow. The three reactive flows used are 50 sccm H_2–100 sccm Ar, 100 sccm C_3H_8 mixture–100 sccm Ar, and 50 sccm air–150 sccm Ar. Fig. 4 shows the NIR thermography image for the base Ar flow and the images taken at the moment of peak temperature change (ΔT) for each reactive flow.

Experiments are conducted numerous times for each sequence of flows. Average maximum temperature changes (ΔT_{max}) for multiple experiments are shown in Table 1. The temperature of the NiO surface under Ar flow (Fig. 4a) for one particular fragment is 724.0 °C. The first reactive flow used is H_2/Ar and led to a ΔT_{max} of −5.2 °C (Fig. 4b). The change is hard to distinguish on the temperature scale used in the image, but is evident in the time series in Fig. 5 that shows changes in the average temperature for a central area of the anode. After the NiO is completely reduced to Ni, the temperature climbs until equilibrating at 721.4 °C. Once the surface is reduced completely, the flow is changed to C_3H_8/Ar (with a total C_3H_8 component of approximately 5% of the flow). During this sustained hydrocarbon fuel flow, the surface temperature immediately drops to 705.0 °C (Fig. 4c) before returning to 716.4 °C. The temperature proceeds to drop slowly from that point as the flow is maintained and carbon continues to form. NiO reduction with H_2 to form Ni and H_2O is slightly exothermic with an equilibrium constant between 10^2 and 10^3 [30], however, the dissociative adsorption of H_2 to form adsorbed H on the Ni surface of Ni/YSZ anodes is endothermic [31]. Considering that the surface of our fragments cools, the hydrogen adsorption process is dominant in our system. Previous studies have shown that hydrocarbon fuels form disordered, likely amorphous, carbon deposits [21] and that the formation of these deposits is endothermic [32,33]. The apparent surface temperature returns to within ~0.5 °C of the initial temperature both after the NiO reduction reaction has completed and after the C_3H_8 flow has been shut off puts a low upper limit on the possible change in emissivity between materials. The data suggest that NiO has a slightly higher emissivity than Ni, which has been previously reported [34].

Table 1
Temperature changes from flow transitions over a Ni/YSZ fragment.

Transition	Avg ΔT_{max} (±) (°C)
Ar to H_2	−5 (2)
H_2 to Air	+23 (3)
Ar to C_3H_8	−19 (2)
H_2 to C_3H_8	−16 (1)
C_3H_8 to Air	+24 (1)

Fig. 4d shows the same cell fragment with carbon deposits at the ΔT_{max} of +23.3 °C while being exposed to air. Two processes are expected to occur while air is flowing: carbon oxidation (combustion with a significant amount of carbon) and nickel oxidation. Initial measurements (in the supplemental material-Figs. S1 and S2) show a ΔT of ~+20 °C when the nickel in the fragment is oxidized. The current set up is such that the carbon deposits cannot be oxidized without also oxidizing the Ni, therefore ΔT_{max} appears to be heating due to both processes.

Fig. 5 shows an average temperature evolution for a portion of the surface during maintained, sequential reactive flows. The Ar–H_2–C_3H_8 sequence shows that the H_2 flow leads to a slight drop in temperature and C_3H_8 leads to a more significant drop, followed by a partial recovery to the initial temperature. In both cases the temperature climbs to a local maximum recovery after 2–3 min. When air is flowed into the chamber the resulting time series has at least four processes that occur based on the four local temperature maxima (marked by asterisks). The first sharp peak is likely the combustion of small particulate carbon that has settled on the surface or elsewhere in the chamber (*i.e.*, the fuel inlet). The second, broad shoulder is attributed to the oxidation of carbon deposits on the surface. The third temperature peak (at ~8 min) is the more intense burning of the smaller carbon deposits throughout the porous anode structure. The final broad maximum that peaks at ~12 min is indicative of the oxidation of the Ni. Ni oxidation is likely occurring throughout the air flow period, however the time at which the maximum temperature is reached is delayed until the carbon is mostly consumed. Furthermore, the effects of carbon and nickel oxidation appear to be additive. Given that the ΔT of the peak assigned to Ni oxidation is approximately double what is observed for Ni oxidation alone, it is likely that carbon oxidation is still occurring and contributing to the ΔT_{max}. Under the maintained air flow, once the carbon and nickel have been oxidized, the temperature begins to return to the initial value. These reactions between surface and atmospheric species are more vigorous than what is seen in working cells, but understanding these processes provides a basis for assigning vari-

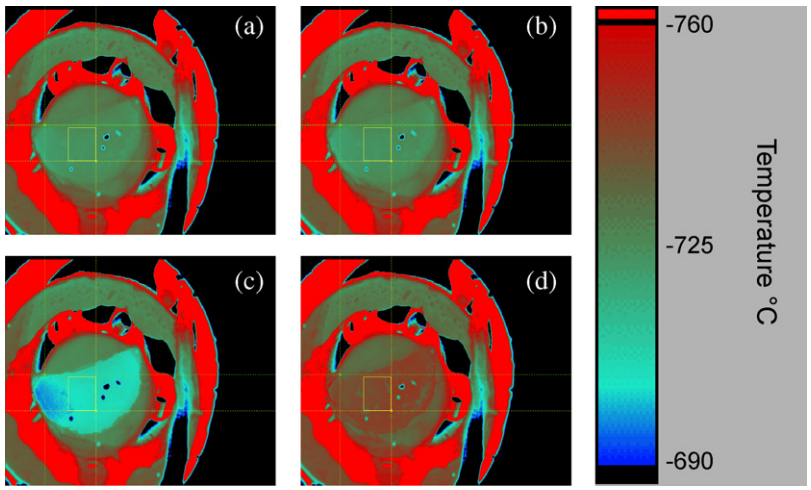

Fig. 4. Images of cell fragments. NIR images of a Ni/YSZ fragment (a) under Ar and at the maximum temperature change after sequential flow changes to: (b) H_2/Ar, (c) C_3H_8/Ar, and (d) air.

ous observations and for more targeted investigations of operating systems.

3.2. Thermal imaging of operating SOFC

The fragment imaging set up is easily converted to handle *in situ* SOFC experiments. Once the anode and cathode lead wires are attached as prescribed above, they are fed between the outer alumina tube and the sapphire window and connected to a potentiostat. The rest of the imaging set up remains unchanged. Two fuels – H_2 and C_3H_8 – are studied *in situ* in this work. In all measurements the furnace is kept at 800 °C, resulting in an initial, baseline, cell surface temperature of 740 ± 10 °C. The variation in the baseline temperature is attributed to heat loss between the center of the furnace and the front access port, which is capped only with a quartz window. The uncertainty associated with the exact placement of the cell for each run is directly responsible for the uncertainty in cell temperature. Each of the fuel sequences described below is conducted multiple times in multiple fuel cell experiments, however, the figures in this section are from one particular sequence for each fuel. The average ΔT_{max} for each process is given in Table 2.

Table 2
Temperature changes from SOFC processes.

Transition	Avg ΔT_{max} (±) (°C)
Ar to H_2	8.6 (0.3)
Polarization, H_2 flow	1.0 (0.6)
Polarization, Ar flow	2.4 (0.5)
H_2 to C_3H_8	−4.0 (0.1)
Polarization, H_2 flow, post C_3H_8	1.5 (0.2)
Polarization, Ar flow, post C_3H_8	2.2 (0.2)

Fig. 6a (red) shows surface heating as a result of flowing a 100 sccm H_2–150 sccm Ar mixture into the anode chamber over an oxidized cermet anode. The ΔT_{max} of +8.1 °C is different than the surface cooling in the fragment study. As noted above, the exothermic $NiO + H_2 \rightarrow Ni + H_2O$ reaction and the endothermic H

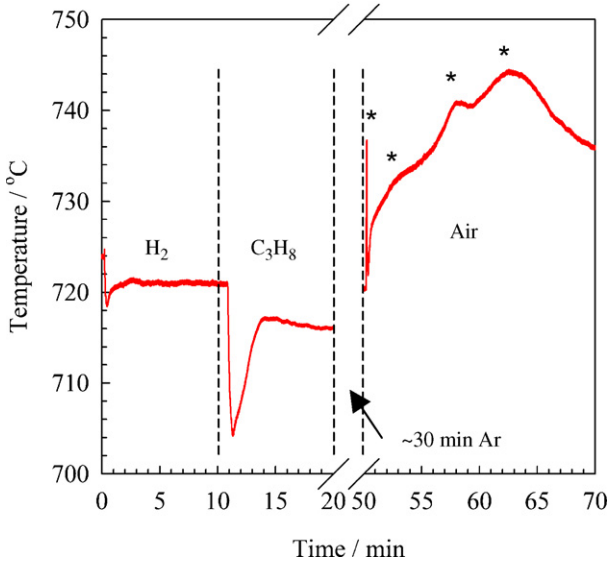

Fig. 5. Cell fragment temperature vs. time. Time series plot of the average temperature of a centralized area on the Ni/YSZ fragment during sequential exposure to: H_2/Ar, C_3H_8/Ar, and air. Local maxima in the air time series are marked by asterisks.

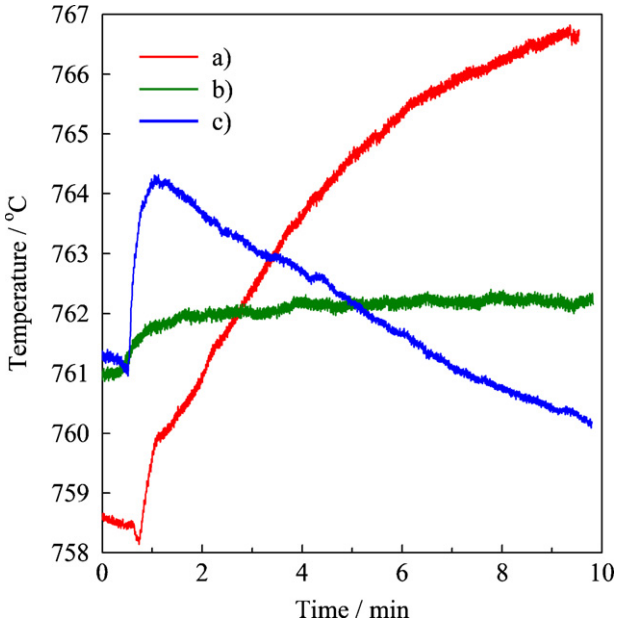

Fig. 6. H_2 SOFC temperature vs. time. Time series plot of the average temperature of a centralized area on the SOFC anode during sequential exposure to: (a) H_2/Ar flow at OCV, (b) H_2/Ar flow while drawing 400 mA, and (c) Ar flow while drawing 400 mA.

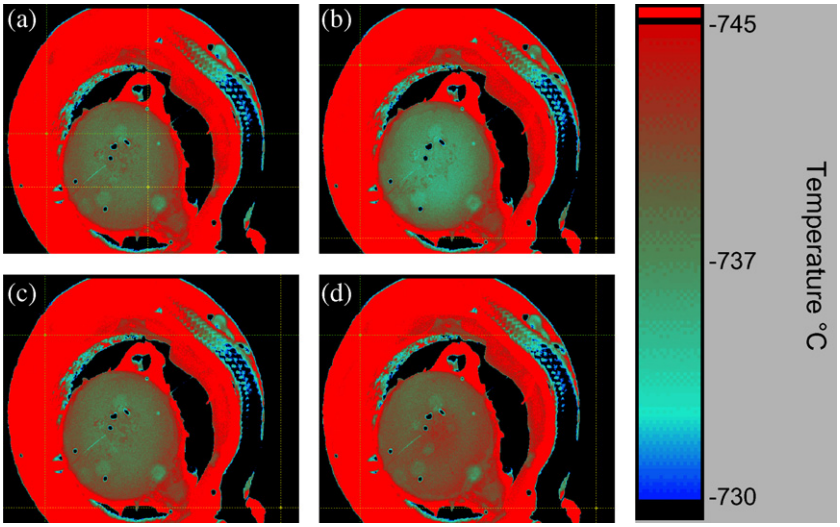

Fig. 7. Images of a SOFC operating with C_3H_8. NIR images of a SOFC anode (a) under Ar and at the maximum temperature changes after the sequential introductions under the following conditions: (b) C_3H_8/Ar flow at OCV, (c) H_2/Ar flow while drawing 400 mA, and (d) Ar flow while drawing 400 mA.

adsorption to the Ni surface are competing; however, unlike the fragment study, there is a source of oxide ions from the cathode that can react with H_{ads}. This would perpetuate the former reaction above and moderate the latter, leading to the temperature increase that is observed. There is no experimental evidence (i.e., a flame or low OCV) to indicate an air leak that would artificially raise the temperature.

The green trace of Fig. 6 (b) shows the anode surface temperature as the cell is polarized under a 20 sccm H_2–150 sccm Ar anode flow. The drop of ~6 °C between the end of the red trace (a) and the beginning of the green (b) trace is due to the change in H_2 flow slowing the reaction between H_2 and NiO. When the cell is polarized such that 400 mA are drawn from the cell (cell voltage of −0.10 V) the temperature immediately climbs, reaching a ΔT_{max} of +1.2 °C, similar to previous reports [18,20]. Fig. 6c (blue) shows the anode surface temperature as the H_2 flow is terminated, but the 400 mA current maintained. The ΔT_{max} is +2.9 °C while the Ni in the cermet is electrochemically oxidized. As the oxidation reaction reaches completion – within a few minutes – the surface cools toward the original temperature as it approaches its initial state.

Fig. 7 shows the anode surface of a cell during a C_3H_8 experiment. When the cell is stable at OCV under a 20 sccm H_2–150 sccm Ar fuel flow (Fig. 7a), the surface temperature is 739.1 °C. Subsequent frames show the cell at OCV with an anode flow of 100 sccm C_3H_8 mixture–150 sccm Ar (Fig. 7b), while drawing 400 mA with a 20 sccm H_2–150 sccm Ar anode flow (Fig. 7c), and while drawing 400 mA with a 150 sccm Ar anode flow (Fig. 7d). The time series of this sequence is shown in Fig. 8, with each change in cell conditions occurring just after time = 0 min.

The red trace in Fig. 8 (a) shows the effect of flowing the C_3H_8/Ar mixture into the anode chamber. C_3H_8 flow leads to rapid carbon deposition and surface cooling. ΔT_{max} from the growth of carbon is −3 °C. This is a factor of 5 less than the drop that is seen in the fragment study. Furthermore, there is no precipitous drop, followed by a recovery close to the initial temperature. Instead, the temperature falls sharply by ~2 °C before a gentler cooling that continues as long as C_3H_8 is flowing and more carbon is deposited. This gentler temperature/time profile is likely due to the presence of other species at or near the anode that would moderate carbon growth, such as oxides that can be replenished by the air flow on the cathode and residual water from the H_2 flow that immediately precedes the C_3H_8 flow. Water and oxides will react with the first carbon species to enter the chamber through the water–gas shift reaction and surface oxidation, respectively. Once carbon species come to dominate the atmosphere of the chamber, carbon deposits can begin to populate the anode surface and cool the cell. The resulting net ΔT in the cell – same as the ΔT_{max}, −3 °C – is comparable to the net ΔT in the fragment experiments (<−5 °C), indicative of an equilibrated carbon growth reaction.

The transition from the C_3H_8/Ar flow to the 20 sccm H_2 flow, shown as the green trace of Fig. 8 (b), leads to the cell temperature heating to 737.2 °C before equilibrating. This trace shows a small, but clear heating to 738.9 °C and a re-equilibration when 400 mA are drawn from the cell (at a cell voltage of −0.12 V). This ΔT is slightly higher than ΔTs that have been modeled and reported for polarized cells in the literature and, as such, is attributed to a combination of polarization and the electrochemical oxidation of carbon under these conditions [18]. However, the H_2 flow will preserve

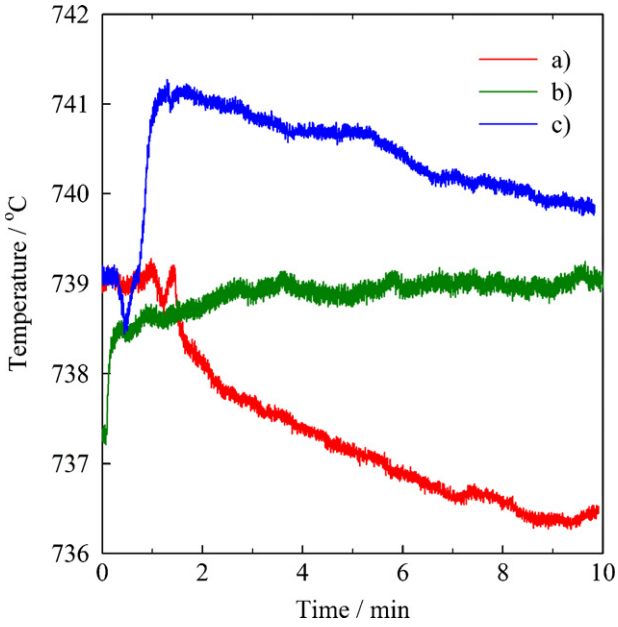

Fig. 8. C_3H_8 SOFC temperature vs. time. Time series plot of the average temperature of a centralized area on the SOFC anode during sequential exposure to: (a) C_3H_8/Ar flow at OCV, (b) H_2/Ar flow while drawing 400 mA, and (c) Ar flow while drawing 400 mA.

most of the carbon deposits on the cell by maintaining the reducing atmosphere on the anode side of the cell. H_2 will also be the primary fuel in this case, reacting with oxides that are being transported through the electrolyte. Given the thickness of the anode, the oxides are more likely to participate in a reaction with the hydrogen fuel close to the anode/electrolyte interface than to propagate through the anode and react with a significant amount of the carbon deposits.

The blue trace of Fig. 8 (c) shows the average surface temperature while the cell current is maintained at 400 mA under Ar, again exposing the carbon deposits and Ni in the anode to a significant oxide flux without other fuels present in the chamber. These conditions result in the carbon deposits and Ni in the anode being the only species available to react with the continued oxide flux. As with carbon and Ni oxidation on the fragments, there appear to be multiple processes displayed in the time series. The two most distinguishable features are at ~2 and ~5 min and are assigned to the times where the electrooxidation of carbon and Ni are most prolific. Again, both processes are thought to be occurring simultaneously, leading to additive heating effects. Unlike the fragment studies, it is not clear which material is oxidized first. In this case the oxidant is the oxide ion. It propagates through the microporous anode by travelling in YSZ particles and presumably has more contact with Ni than carbon. However, it cannot be determined if the deposits have overgrown the Ni particles, making contact with YSZ. Nevertheless after 10 min under these conditions the anode temperature is falling and the surface appears green, indicating a clean and oxidized anode surface. The ΔT_{max} of the oxidation time series in the operating SOFC is only +3.5 °C, approximately 20 °C less than what is seen in the fragment studies. This lower heating shows clearly that atmospheric oxidation (i.e., combustion) is faster and more intense than the electrochemical oxidation that occurs in an operating fuel cell.

4. Conclusions

This work demonstrates the ability to spatially and temporally map SOFC anode temperatures in operating cells. A Si-CCD camera-based NIR imagining system is demonstrated first on fragments of Ni/YSZ cermet anodes. It is found that NiO reduction to Ni and carbon deposition cool the fragment surface by 5.2 and 16.4 °C, respectively. When air is flowed over the fragments, the temperature time series shows that as many as four processes occur as carbon deposits and the Ni are oxidized, and there is evidence that the temperature effects of the two processes are additive. In operational cells, the temperature changes are damped. The drop in temperature with carbon deposition is only 3 °C due to the presence of oxides and water in working SOFCs. Electrochemical oxidation of carbon deposits results in a ΔT of +1.7 °C, which demonstrates that oxidation by the oxide flux is less vigorous than atmospheric oxidation. This NIR technique is significantly cheaper, more sensitive, and less cumbersome than mid-IR imaging systems, providing a quick-and-easy way to characterize operating SOFCs and identify the processes occurring under various conditions. Future work will focus on developing experiments and theoretical models to explore other fuels and cell architectures to determine how changes in conditions, including the humidification of fuel flows, may affect the temperature of the cell and, in turn, cell performance and stability. Ongoing investigations include coupling thermal imaging with *in situ* Raman spectroscopy to identify the species responsible for the temperature changes observed during various operating conditions.

Additional information, including larger-sized versions of Figs. 4 and 7, is available in supplemental material.

Acknowledgements

Support for this work was provided by the Office of Naval Research. M.B.P. acknowledges the National Research Council, Naval Research Laboratory Postdoctoral Fellowship program. The authors acknowledge Karen E. Swider-Lyons and Jeremy J. Pietron at NRL for equipment use, and Professors Bryan W. Eichhorn and Robert A. Walker at the University of Maryland, College Park for helpful discussions.

Appendix A. Supplementary data

Supplementary data associated with this article can be found, in the online version, at doi:10.1016/j.jpowsour.2009.06.072.

References

[1] K. Alanne, A. Saari, V.I. Ugursal, J. Good, J. Power Sources 158 (2006) 403–416.
[2] A. Atkinson, S. Barnett, R.J. Gorte, J.T.S. Irvine, A.J. McEvoy, M. Mogensen, S.C. Singhal, J. Vohs, Nat. Mater. 3 (2004) 17–27.
[3] F. Calise, A. Palombo, L. Vanoli, J. Power Sources 158 (2006) 225.
[4] E. Fontell, T. Phan, T. Kivisaari, K. Keranen, J. Fuel Cell Sci. Technol. 3 (2006) 242–253.
[5] R.M. Ormerod, Chem. Soc. Rev. 32 (2003) 17–28.
[6] J.B. Goodenough, Annu. Rev. Mater. Res. 33 (2003) 91–128.
[7] J.B. Goodenough, Rep. Progr. Phys. 67 (2004) 1915–1993.
[8] F.Z. Chen, S.W. Zha, J. Dong, M.L. Liu, Solid State Ionics 166 (2004) 269–273.
[9] A.L. Dicks, J. Power Sources 71 (1998) 111–122.
[10] N. Laosiripojana, S. Assabumrungrat, J. Power Sources 163 (2007) 943–951.
[11] R.J. Kee, H. Zhu, A.M. Sukeshini, G.S. Jackson, Combust. Sci. Technol. 180 (2007) 1207–1244.
[12] J. Dong, Z. Cheng, Z. Shaowu, M. Liu, J. Power Sources 156 (2006) 461–465.
[13] X. Lu, P.W. Faguy, M. Liu, J. Electrochem. Soc. 149 (2002) A1293–A1298.
[14] O.S.N. Sum, E. Djurado, T. Pagnier, N. Rosman, C. Roux, E. Siebert, Solid State Ionics 176 (2005) 2599–2607.
[15] S. Bebelis, S. Neophytides, Solid State Ionics 152/153 (2002) 447–453.
[16] A. Bieberle, L.P. Meier, L.J. Gauckler, J. Electrochem. Soc. 148 (2001) A646–A656.
[17] H.W. Abernathy, E. Koep, C. Compson, Z. Cheng, M.L. Liu, J. Phys. Chem. C 112 (2008) 13299–13303.
[18] D.J.L. Brett, P. Aguiar, R. Clague, A.J. Marquis, S. Schottl, R. Simpson, N.P. Brandon, J. Power Sources 166 (2007) 112–119.
[19] Z. Cheng, M.L. Liu, Solid State Ionics 178 (2007) 925–935.
[20] J. Gang, K. Reifsnider, H. Xinyu, J. Fuel Cell Sci. Technol. 5 (2008), 031006-031001-031006.
[21] M.B. Pomfret, J. Marda, G.S. Jackson, B.W. Eichhorn, A.M. Dean, R.A. Walker, J. Phys. Chem. C 112 (2008) 5232–5240.
[22] M.B. Pomfret, J.C. Owrutsky, R.A. Walker, Anal. Chem. 79 (2007) 2367–2372.
[23] Q.H. Wu, H. Abernathy, Z. Cheng, M.L. Liu, Asia-Pacific Conference on Surface Science and Engineering, World Scientific Publ Co Pte Ltd., Hong Kong Peoples R China, 2006, pp. 587–591.
[24] F. Meriaudeau, Image Vision Comput. 25 (2007) 1124–1133.
[25] J.C. Owrutsky, D.A. Steinhurst, C.P. Minor, S.L. Rose-Pehrsson, F.W. Williams, D.T. Gottuk, Fire Saf. J. 41 (2006) 315–320.
[26] T. Saito, S. Sakai, I. Iizawa, E. Suda, K. Umentani, K. Kaneko, Y. Furukawa, T. Ohkura, Earth Planets Space 57 (2005) e5–e8.
[27] G. Zauner, D. Heim, G. Hendorfer, K. Niel, in: M.A. Hunt, J.R. Price (Eds.), SPIE-IS&T Electronic Imaging, 2003, pp. 283–290.
[28] G. Zauner, D. Heim, K. Niel, G. Hendorfer, H. Stoeri, in: J.R. Price, F. Meriaudeau (Eds.), SPIE-IS&T Electronic Imaging, 2004, pp. 81–89.
[29] F. Zhao, A.V. Virkar, J. Power Sources 141 (2005) 79–95.
[30] J.T. Richardson, R. Scates, M.V. Twigg, Appl. Catal. A 246 (2003) 137–150.
[31] J. Mukherjee, S. Linic, J. Electrochem. Soc. 154 (2007) B919–B924.
[32] M. Cimenti, J.M. Hill, J. Power Sources 186 (2009) 377–384.
[33] L.M. Wagg, G.L. Hornyak, L. Grigorian, A.C. Dillon, K.M. Jones, J. Blackburn, P.A. Parilla, M.J. Heben, J. Phys. Chem. B 109 (2005) 10435–10440.
[34] Raytek Emissity Table for Metals, 2008, http://www.raytek.com/Raytek/en-r0/IREducation/EmissitivityTableMetals.htm.